

Additive Manufacturing of Compliant Mechanisms for Deployable Aerospace Structures

A Thesis
Presented to
The Academic Faculty
By

Christine A. Gebara

In Partial Fulfillment
of the Requirements for the Degree
Master of Science in Aerospace Engineering

Georgia Institute of Technology

May 2021

Additive Manufacturing of Compliant Mechanisms for Deployable Aerospace Structures

Approved by:

Professor Julian J. Rimoli, Advisor
School of Aerospace Engineering
Georgia Institute of Technology

Professor Claudio V. Di Leo
School of Aerospace Engineering
Georgia Institute of Technology

Dr. Samuel Case Bradford V
Small Spacecraft and Payload Mechanical
Engineering
*Jet Propulsion Laboratory, California
Institute of Technology*

Dr. R. Peter Dillon
Materials Development & Manufacturing
Technology
*Jet Propulsion Laboratory, California
Institute of Technology*

Date Approved: April 22, 2021

*To my family, friends, and colleagues,
who supported me and heard a lot about springs.*

*Specifically, to my Dad,
who has never stopped encouraging me.*

ACKNOWLEDGEMENTS

This work would not be possible without the guidance of many JPL mechanical engineers who continuously push the forefront of space exploration. Specific thanks go to Paul Lytal, the delivering cognizant engineer for the SWOT and NISAR boom hinge mechanisms. Further, Andre Pate was instrumental in the manufacturing of test articles. Dr. Case Bradford was continuously supportive of this research, despite many hurdles. Special thanks to Dr. Julian J Rimoli who has served as a mentor and advisor both inside and outside of technical environments.

The research described in this report was carried out at the Jet Propulsion Laboratory, California Institute of Technology under a contract with the National Aeronautics and Space Administration.

TABLE OF CONTENTS

ACKNOWLEDGEMENTS.....	iv
LIST OF TABLES.....	vii
LIST OF FIGURES.....	viii
NOMENCLATURE.....	x
SUMMARY.....	xi
CHAPTER 1 INTRODUCTION.....	1
CHAPTER 2 BASIS AND BACKGROUND.....	2
2.1 Additive Manufacturing within the Aerospace Industry	2
2.2 State of the Art in Deployable Spacecraft Structures.....	4
CHAPTER 3 Traditional Mechanism.....	5
3.1 Traditional Mechanism Design and Fabrication.....	6
3.2 Mechanism Integration and Hardware Failure.....	9
3.3 Mechanism Modification.....	11
3.4 Resolution for Traditional Mechanisms.....	12
CHAPTER 4 SPRING THEORY	14
4.1 Spring Design Methodology.....	14
4.2 Spring Design Considerations.....	15
4.3 Spring Design Software.....	15
CHAPTER 5 DESIGN FOR ADDITIVE MANUFACTURING.....	16
5.1 Material and Process Selection.....	16
5.2 Spring Design.....	17
CHAPTER 6 MANUFACTURING AND TESTING.....	19
6.1 Manufacturing Preparation.....	19
6.2 Manufacturing and Inspection.....	19
6.3 Experimental Test Setup.....	23
6.4 Torque and Life-Cycle Testing Results.....	23
6.5 Material Testing.....	25
CHAPTER 7 FUTURE IMPLICATIONS.....	27
APPENDIX A: DRAWINGS.....	30

APPENDIX B: ADVANCED SPRING DESIGN SOFTWARE.....	33
APPENDIX C: AM MATERIAL COMPARISON.....	34
REFERENCES.....	35

LIST OF TABLES

Table 1. Summary of hardware failure investigation testing.....	11
Table 2. Traditional flight hardware material compared to AM EOS MS1.....	16
Table 3. Summary of design variables for springs tested.....	18
Table 4. Spring Torque Performance Test Results.....	24
Table 5. Tensile test result summary.....	25
Table 6. Material comparison.....	34

LIST OF FIGURES

Figure 1.	Aerojet Rocketdyne Bantam rocket engine and SpaceX Merlin rocket engine.....	3
Figure 2.	PIXL Instrument with AM hardware on Mars.....	4
Figure 3.	JPL RainCube satellite and the Planetary Society’s LightSail 2 on orbit.....	4
Figure 4.	SWOT hinge locations and NISAR hinge locations shown.....	5
Figure 5.	Hinge deploy & latching mechanisms (NISAR hinge shown).....	6
Figure 6.	View of NISAR and SWOT spring mechanisms demonstrating differences in overall length and relaxed spring arm position.....	7
Figure 7.	Torsion Spring on CNC Coiling Machine.....	7
Figure 8.	Cross section of NISAR Spring Mechanism.....	8
Figure 9.	Image of spring mechanism during thermal testing with hardware Failure circled.....	9
Figure 10.	Sleeve bearing showing wear and self-contact after disassembly, first failed sleeve bearing shown with spring, and second failed sleeve bearing with spring removed.....	10
Figure 11.	Torque profile of mechanism as it is wound and unwound. Blue indicates initial cycles, yellow intermediate cycles, and red represents later cycles.....	12
Figure 12.	As printed springs from Vendor #1 shown before support material removal.....	20
Figure 13.	Vendor #1 spring (left) and Vendor #2 spring (right).....	20
Figure 14.	Defects upon inspection of a spring from AM Vendor 1.....	21
Figure 15.	Defects upon inspection of a spring from AM Vendor 2.....	21
Figure 16.	Dimensional inspection of cross section error for spring winding width. This inspection demonstrates that most as-fabricated springs achieve required geometric tolerances for winding width.....	22
Figure 17.	Inspection of spring major dimensions. This inspection demonstrated that all AM parts as fabricated achieve required geometric tolerances for major dimensions.....	22

Figure 18.	Experimental test setup for measuring spring torque performance.....	23
Figure 19.	Average spring torque output with respect to displacement.....	25
Figure 20.	Tensile coupons shown as printed and after machining.....	26
Figure 21.	Flight spring design compared to zero stress margin AM spring design.....	27
Figure 22.	Structurally embedded spring with nine total parts demonstrates reduction in part count when compared to traditional manufacturing methods.....	28
Figure 23.	AM Spring Drawing.....	30
Figure 24.	AM Structurally Embedded Spring Drawing.....	31
Figure 25.	AM enabled spring mechanism drawing.....	32
Figure 26.	Advanced Spring Design Software.....	33

NOMENCLATURE

<i>AM</i>	= Additive Manufacturing	<i>l</i>	= Length
<i>c</i>	= Distance from neutral axis	<i>LENS</i>	= Laser-Engineered Net Shaping
<i>C</i>	= Spring Index	<i>LPBF</i>	= Laser Powder Bed Fusion
<i>CTE</i>	= Coefficient of Thermal Expansion	<i>M</i>	= Applied Moment
<i>D</i>	= Diameter	<i>MOXIE</i>	= Mars Oxygen In-Situ Resource Utilization Experiment
<i>DED</i>	= Direct Energy Deposition	<i>N</i>	= Number of Coils
<i>E</i>	= Elastic Modulus	<i>NASA</i>	= National Aeronautics and Space Administration
<i>EOS</i>	= Electro Optical Systems	<i>NISAR</i>	= NASA-ISRO Synthetic Aperture Radar
<i>F</i>	= Force	<i>PFR</i>	= Problem Failure Report
<i>FS</i>	= Factor of Safety	<i>PIXL</i>	= Planetary Instrument for X-ray Lithochemistry
<i>I</i>	= Moment of Inertia	<i>r</i>	= Radius
<i>k</i>	= Spring Rate	<i>SWOT</i>	= Surface Water and Ocean Topography
<i>K</i>	= Wahl Stress Concentration Factor	<i>U</i>	= CubeSat Unit (10cm x 10 cm x 10cm)
<i>ISARA</i>	= Integrated Solar Array and Reflectarray Antenna	σ	= Stress
<i>ISRO</i>	= Indian Space Research Organization	θ	= Angular deflection
<i>JPL</i>	= Jet Propulsion Laboratory		

SUMMARY

In the past 10 years, complex deployable structures have become common on JPL CubeSats (e.g. RainCube, MARCO, ISARA) and large-scale spacecraft (e.g. SMAP, SWOT, NISAR, Starshade). As new, ambitious missions are pursued, there is an increased need for more mass and volume efficient deployments (higher packing density). Over the same timeframe, additive manufacturing (AM) has enabled the fabrication of new forms of flight hardware including the PIXL instrument structure, the Moxie instrument, and the RainCube antenna structure. However, AM of compliant mechanisms has not been leveraged to design deployable space structures.

AM of compliant mechanisms within deployable structures (e.g. antennas, solar panels, booms), could drastically lower part counts, create novel structural tuning methods, and design previously impossible geometries. Utilizing AM would therefore lead to deployable spacecraft elements with higher mass and volume efficiencies.

AM of compliant mechanisms (4D printing) is an active research area. The ability to print these mechanisms in polymers has been demonstrated. However, metal 4D-printing is still a maturing technology for aerospace applications. One area of interest is additive manufacturing of flexure hinges for flat reflectarray antennas, radiators, and solar panels. Another application is the ability to print structurally embedded spring elements that are geometrically tuned for a specific deployable structure. This could result in numerous benefits. Primarily, embedding compliant mechanisms directly where they are used would simplify deployment dynamics, thus also simplifying the characterization and control of the deployment. Second, printing structurally embedded compliant elements could enable systems that are otherwise impossible to assemble or manufacture. For example, the ability to print a structurally embedded torsional spring within the hinge mechanisms for a SWOT-type deployable mast could ease manufacturing problems, decrease part count, decrease mechanism shimming, and improve reliability.

CHAPTER 1

INTRODUCTION

With the development of additive manufacturing (AM), fabrication constraints have relaxed. It is now possible to manufacture new types of geometries, materials, and components not otherwise possible with subtractive manufacturing. This progress enables a new class of space systems to be imagined. Furthermore, the infusion of AM into industry has corresponded with deployable aerospace structures becoming increasingly common on spacecraft of all sizes. Deployable structures often require many small parts and compliant mechanisms to actuate deployment. AM can be leveraged to minimize part count, mass, and volume of deployable structures. For example, compliant elements (e.g., spring and flexures) can be embedded within surrounding structural elements as opposed to being joined, bonded, or otherwise mechanically connected. Though various AM methods have differing restrictions on possible part size, the ability to print large, monolithic deployable aerospace structures is soon on the horizon. To achieve the ultimate goal of being able to additively manufacture entire spacecraft systems, development of AM compliant elements must be studied at the component and subsystem level to allow for the technology to mature. This report will take an existing deployable structure mechanism and modify the design to leverage the benefits of additive manufacturing.

CHAPTER 2

BASIS AND BACKGROUND

Additive manufacturing began in the early 1980's and focused primarily on polymer materials. In the early 1990's, additive manufacturing of metals originated on Optomec's Laser-Engineered Net Shaping (LENS) metal powder system. This original process was based on technology developed by Sandia National Labs. [1] Since, many forms of AM have emerged for both polymers and metals. Over the past decade, several processes for AM of metals have matured into wide-spread production methods used around the world in numerous industries.

2.1 Additive Manufacturing within the Aerospace Industry

Additive manufacturing within aerospace engineering, and, more specifically, spacecraft design, has been adopted slowly relative to other industries for critical applications. [1] The fact that additively manufactured parts cannot be analyzed using traditional material properties has made aerospace organizations hesitant to infuse the technology. AM hardware is subject to different process complications that will be discussed later in this document. However, there have been some notable successes in infusing additive manufacturing into space hardware. Aerojet Rocketdyne and SpaceX have both successfully additively manufactured small rocket engines. Aerojet's Bantam rocket engines are assembled with only three primary components: the injector assembly, the combustion chamber, and a monolithic throat and nozzle section. All the components are made using AM. [2] Furthermore, SpaceX has successfully launched a 3D-printed main oxidizer valve in a Merlin 1D engine. [3] In both of these examples, the motivation to print this hardware was to reduce part count, decrease weight, shorten manufacturing time, and increase reliability. This hardware is shown in Figure 1.

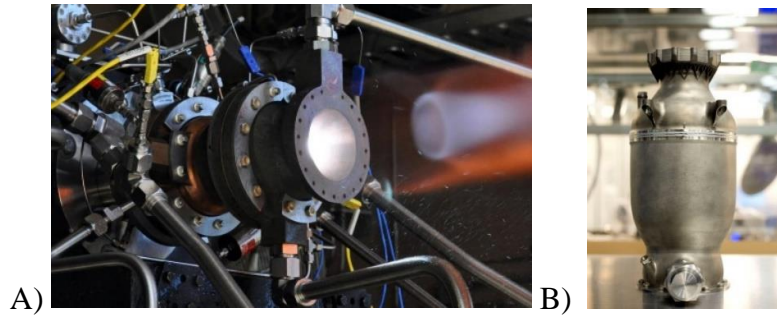


Figure 1. A) Aerojet Rocketdyne Bantam rocket engine [2] B) SpaceX Merlin rocket engine. [3]

NASA’s Jet Propulsion Laboratory (JPL) has also been on the forefront of infusing additive manufacturing into space flight in various applications. The ability to print components composed of numerous metals is especially interesting because of the ability to tune thermal expansion properties across a single component. These are often referred to as “functionally graded” components. Additionally, the ability to print geometries not otherwise possible using traditional manufacturing techniques is another advantage of additive manufacturing. For example, topology optimization allows a structure design to be optimized based on expected loading conditions. This optimal design solution often results in complicated structures that are impractical to fabricate using subtractive manufacturing. However, in some instances, AM has enabled these optimized structures to be manufactured. Project Gamma is an example of a planetary lander that has been designed using topology optimization and generative design. This lander was designed by JPL in partnership with Autodesk. [4] In another practical example, the JPL Perseverance Rover has landed on Mars with numerous additively manufactured parts. Both the Planetary Instrument for X-Ray Lithochemistry (PIXL) and Mars Oxygen In-Situ Resource Utilization Experiment (MOXIE) have components that are manufactured using AM. Specifically, the PIXL instrument benefited from shorter lead times, cheaper costs, and increased reliability by utilizing AM. [5]

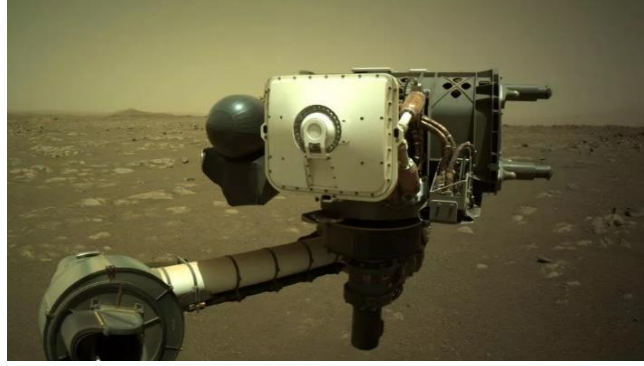


Figure 2. *PIXL Instrument with AM hardware on Mars. [6]*

2.2 State of the Art in Deployable Spacecraft Structures.

Deployable space structures are utilized for numerous applications including space-based antennas, radiators, solar panels, sun shades, and optics. The James Webb Telescope has tens of articulated deployments including the large solar shield and primary mirror subsystems. This includes antennas and a large, multi-layer solar shield. On a smaller scale, deployable structures contribute to increasing the functionality of the CubeSat form factor. JPL's RainCube Satellite was able to deploy a 0.5m parabolic Ka-Band antenna from a 2-unit CubeSat canister. [7] The Planetary Society also successfully deployed a 34 square meter solar sail from a 3U form factor with boom lengths of 4m during the LightSail 2 mission. [8] Figure 3 displays images of these missions in their deployed state. Deployable structures in the past decade have heavily leveraged composite materials, compliant mechanisms, and spring elements. For example, deployable booms are often comprised of rolling tape springs fabricated with carbon fiber composites or spring steel. [9]

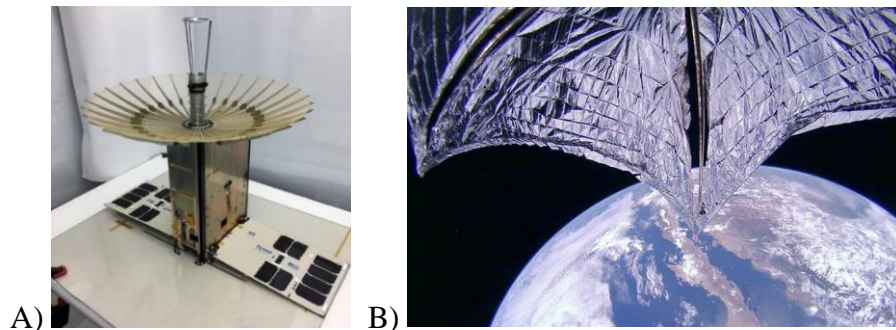


Figure 3. *A) JPL RainCube satellite [7] and B) the Planetary Society's LightSail 2 on orbit [8]*

CHAPTER 3

Traditional Mechanism

NASA's Jet Propulsion Laboratory is currently developing two earth orbiting satellites. The Surface Water Ocean Topography (SWOT) mission will conduct the first global survey of Earth's surface water. [10] The NASA-ISRO Synthetic Aperture Radar (NISAR) mission will study temporal changes to Earth's land and ice-sheets using advanced radar techniques. [11] Both missions serve to understand how the Earth is changing over time using radar-based instruments.

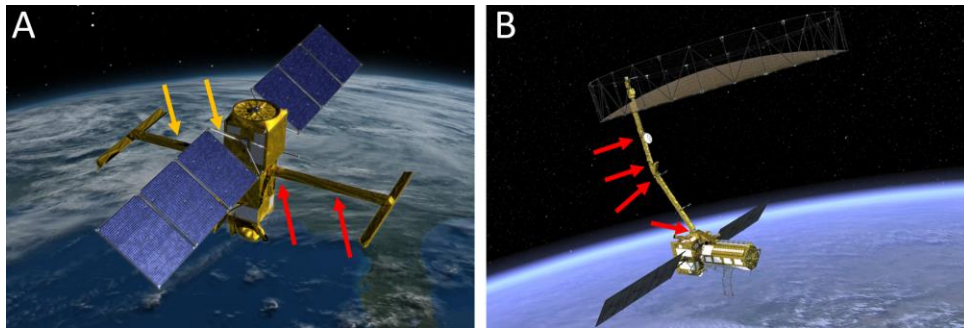


Figure 4. A) SWOT hinge locations [10] and B) NISAR hinge locations shown. [11]

Both SWOT and NISAR use deployable radar reflector mast designs developed at JPL. These deployable masts, while different in geometry, have similar components and sub-assemblies. Both masts are constructed from bonded Invar and carbon fiber composite structures and employ analogous flight deployable hinge mechanisms. The SWOT mission has two identical reflector masts, each with two deployable hinges. NISAR has a single mast with four deployable hinges. These masts can be seen in Figure 4. Operationally, the deployable masts are launched in a stowed state with a launch restraint system composed of separation nut devices. When commanded, the launch restraints release a pre-tensioned spring and damper mechanism which deploys each hinge. Hinge deployment progress is monitored on the ground using a potentiometer as well as a limit switch on each hinge. Upon completion of the deployment, an actuator-driven latching mechanism preloads precision alignment features on either side of the hinge together. Figure 5 displays an overview of the mechanisms.

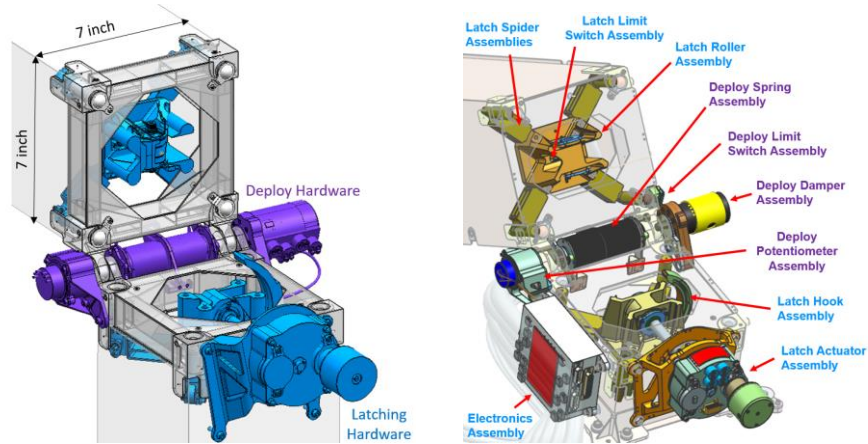


Figure 5. Hinge deploy & latching mechanisms (NISAR hinge shown).

3.1 Traditional Mechanism Design and Fabrication

Each deployable hinge for the SWOT and NISAR masts is outfitted with a spring, damper, and potentiometer mounted co-axially with each hinge line. The NISAR mast is composed of 7-inch square composite tubing. The SWOT mast is composed of 10-inch square composite tubing. Figure 6 displays the spring mechanisms for each mission. The smaller 7-inch mast cross-section of NISAR became the driving factor in the design of the spring mechanism to maximize mechanical commonality between projects. Common mounting interfaces were designed for both projects. Ultimately, this led to a cylindrical volume allowance of 7 inches in length and 1.75 inches in diameter for the NISAR spring mechanism. Because of the differences between the SWOT and NISAR stowed hinge angles, as well as differences in hinge angles at different locations on each mast, 4 different torsion spring configurations were developed, each with the spring arms located at different angles relative to each other in the relaxed position. This can also be seen in Figure 6 when comparing both images.

The spring mechanism is required to meet JPL design requirements for mission critical spring design. As such, springs are required to have a minimum ‘no test’ yield factor of safety (FS) of 1.50 and an ultimate FS of 1.65. Furthermore, JPL design principles impose a minimum mechanism torque margin of 100% in worst case environments at end of life. These driving requirements meant the torsion springs needed to produce a minimum deployment-direction torque of 28 inch-pounds at hinge closure. A standard round wire 17-7 precipitation-hardened stainless-steel torsion spring would not produce adequate torque in the volume available without violating

mission critical factors of safety. Alternative materials such as Elgiloy and MP35N were considered, but all vendors considered for fabrication of these springs had a significantly higher volume of experience working with 17-7 stainless steel, and developmental risk was deemed higher with these alternative materials. Therefore, a geometric solution was developed: a rectangular cross section spring to maximize the moment of inertia within the available volume.

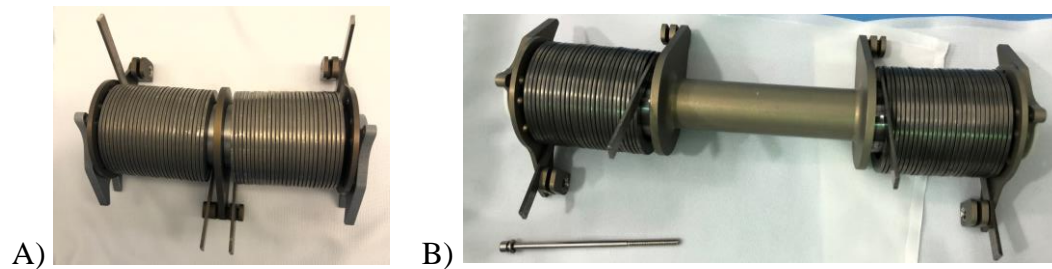


Figure 6. View of A) NISAR and B) SWOT spring mechanisms demonstrating differences in overall length and relaxed spring arm position.

After developmental fabrication test runs, the spring wire height-to-width ratio selected for the spring cross section was 3.88:1. This value was determined to be the highest ratio achievable with available CNC spring winding manufacturing capabilities. Spring manufacturing still included many challenges given the propensity of the spring wire to rotate about the axis of the wire during winding and inconsistencies in spring back, resulting in non-uniform torsion spring inner and outer diameters. The CNC spring winding configuration is shown in Figure 7. Guide support features were added to the flight spring mandrel design to prevent twist about the axis of the spring wire at either end of each spring.

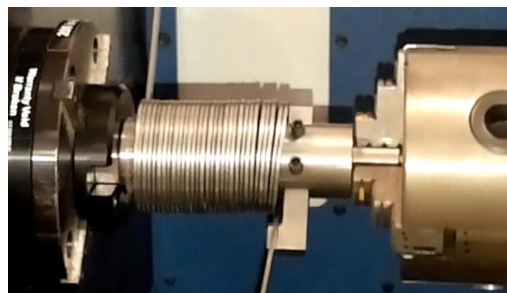


Figure 7. Torsion Spring on CNC Coiling Machine.

The rectangular cross section caused early manufacturing issues for the flight units. The springs initially exceeded axial length requirements. Furthermore, the wire was prone to unexpected twisting during winding. The initial inclination of the team was to attempt to relax the overall spring length requirement, but that would have had significant ripple impacts into the mature design of the hinge and mast structures. To address length requirement non-compliance, the initially-baselined spring with 29 coils was modified to a baseline design of 27 coils. With this change, however, the spring violated JPL design requirements for minimum factor of safety. Reducing the number of windings increased the stress in the spring. In consultation with JPL materials experts, material coupon testing for the flight lot of material was conducted to establish higher strength allowables for the hardware to address the slight negative strength margins. Ultimately, the final flight springs were successfully manufactured with a variation of less than 0.007 inches in diameter and 0.012 inches in length across twenty-eight units. The torsion spring design that was developed met all requirements, as verified via tensile test witness coupons of the material, destructive winding testing, dye penetrant inspection, and other verification techniques.

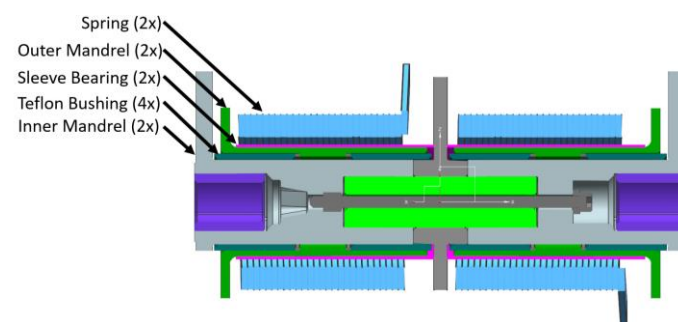


Figure 8. *Cross section of NISAR Spring Mechanism.*

Once the spring mechanism design solution was reached, prototype units were built. A prototype test program was successfully completed prior to flight hardware fabrication to reduce the risk of issues in the flight hinge and latching mechanism development. The prototype test program included both ambient and thermal functional testing and thermal characterization testing on a flight-like hinge fixture. The prototype program did not include vibrational testing or life

testing due to programmatic constraints. The lack of these prototype tests prevented design issues described in the next section from being uncovered prior to integration of the final flight units.

3.2 Mechanism Integration and Hardware Failure

Upon successful completion of the prototype test program, fabrication of qualification, flight spare, and flight piece parts ensued. Seven SWOT spring mechanisms were assembled with a qualification unit slated for thermal testing to characterize torque output at the worst case cold, ambient, and hot qualification temperatures. The qualification unit was of a SWOT design, but was deemed similar to the NISAR design. Therefore, a single qualification unit was used for both missions. Thermal life testing was conducted after the qualification unit had undergone vibrational testing. Thermal test temperatures and vibrational test levels were set to encompass the environments for both missions.

During thermal testing, the spring was wound and unwound manually through its operational range of motion using a rotary turn table. Torque output and rotary angle were tracked with a transducer and encoder, respectively. At the qualification hot temperature, hardware failure was observed. From repeated torsion spring cycling (winding and unwinding), fragmented Teflon Foreign Object Debris (FOD) was generated. This can be seen in Figure 9. The source of the FOD was determined to be from two glass-filled Teflon sleeve bearings in contact with the inner diameter of each spring inside the mechanism. The spring mechanism continued to function and torque performance was not measurably altered by the fragmentation. Upon further investigation, it was determined that the sleeve bearing had begun to fail prior to hot thermal testing.

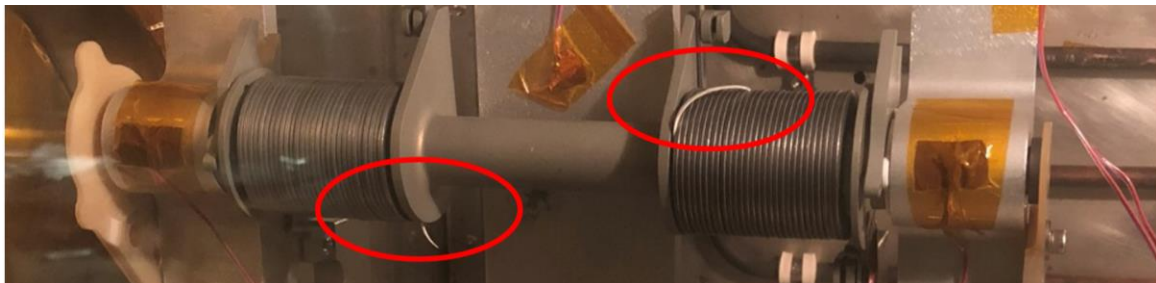


Figure 9. Image of spring mechanism during thermal testing with hardware failure circled.

After the failure, the qualification spring mechanism was disassembled. The root cause was identified to be invalid analytical model simplification. The analytical model simplified the torsion spring geometry as a cylinder with uniform inner diameter. The real rectangular cross section torsion springs had slight variations in the inner diameter between coils, with sharp cutting edges presented to the Teflon bushings during cycling. Therefore, the contact stress in the real hardware at the cutting edge was substantially higher than in the idealized analytical model. In addition, the sleeve bearing had been designed with a helical cut along the axis of the bearing, designed to allow radial compliance as the torsion spring inner diameter changes during winding/unwinding operations. However, the helical cut also drastically reduced axial stiffness of the part. As such, when the spring coils moved axially during winding, the edges of the bushing began to contact each other and plastically deform. These failures can be seen in Figure 10.

This failure resulted in the opening of a JPL Problem Failure Report (PFR). As such, a technical team was assembled to oversee the investigation and resolution of the failure. Because of the multi-mission applicability of the hardware design, the team was composed of representatives from both the SWOT and NISAR projects. Any resulting actions needed to be approved by both missions. There was programmatic motivation to utilize as much of the existing hardware as possible.

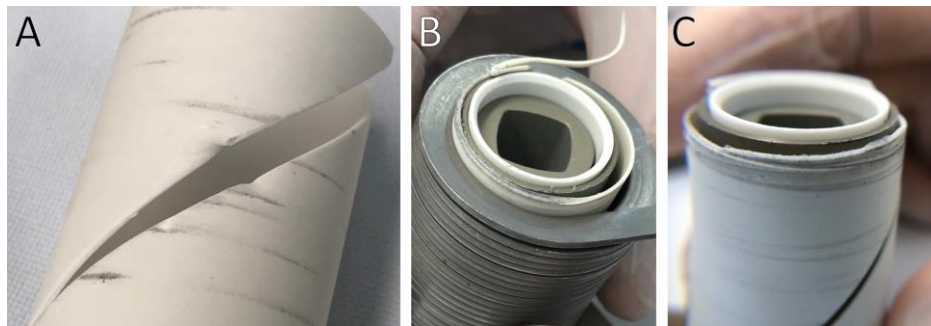


Figure 10. A) Sleeve bearing showing wear and self-contact after disassembly, B) first failed sleeve bearing shown with spring, and C) second failed sleeve bearing with spring removed.

3.3 Mechanism Modification

Ultimately, a solution was developed that replaced the Teflon sleeve bearing with a grease-plated 440C stainless steel sleeve bearing with modified geometry. Over 400 functional cycles and 20 disassembly procedures of the qualification mechanisms were carried out during the hardware failure investigation. Table 1 summarizes the test campaign that was conducted to find a new sleeve bearing design. The fundamental approach was to change one parameter at a time from the original bushing design and evaluate its effect on the health of the component and test performance until an acceptable solution was found. An acceptable solution had to simultaneously meet mechanism torque performance needs as well as avoid significant FOD generation or damage to the bushing through three times the planned number of flight unit life cycles.

Table 1. Summary of hardware failure investigation testing.

Index	Material	Bearing Design	Test Type	Test Result	Notes
1	Teflon	Helical Cut	Vibrational, Thermal, Cycle Life	Fail	-Initial Failure
2	6061		Torque Characterization	Fail	-Torque requirement failure
3	304C		Torque Characterization	Fail	- Noise from mechanism -Torque requirement failure - Helical cut deemed unacceptable
4	Bronze	Solid Sleeve Bearing	Torque Characterization	Fail	- FOD found
5	440C		Torque Characterization	Fail	- FOD Found
6	Copper	Extended, solid sleeve bearing	Torque Characterization	Fail	- FOD found - Torque requirement failure
7	440C		Torque Characterization, Cold	Pass	- Noise witnessed - Good Torque
8	Bronze		Torque Characterization	Fail	- FOD found - Good torque
9	440C		Vibe, Cold, Hot, Cycle Life	Pass	- Full Life Test - Good Torque - Noise witnessed
10	440C		Torque Characterization	Pass	- Confirm lubricant alleviates noise

As described previously, torque testing of the mechanism included using a transducer and encoder to measure torque and rotational position, respectively. This torque testing was carried out for each potential bushing design. If the torque was deemed acceptable, the unit was then disassembled and inspected for any FOD or other potential failures. Figure 11 displays the torque

performance of the spring mechanism for the final bushing design in ambient and cold conditions during cycle life testing (defined as at least three times the expected number of mechanism cycles). Torque performance is seen to degrade up to 10 in*lbs over the course of 30 cycles at ambient conditions. Furthermore, torque performance degrades at cold temperature about 10 in*lbs. Despite performance degradation, torque never violated the 28 in*lbs torque requirement. Also notable is the fact that the unwinding torque at cold temperature is seen to be nearly constant. This differs from the analytical model of linearly decreasing torque. The cause for near-constant torque is suspected to be internal mechanism friction caused by migration and degradation of lubricant on the bushing as it is cycled.

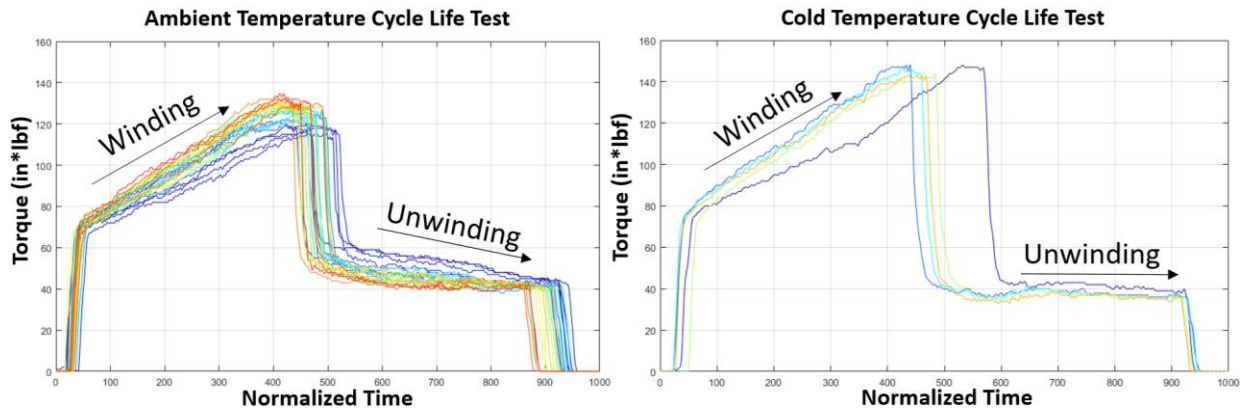


Figure 11. Torque profile of mechanism as it is wound and unwound. Blue indicates initial cycles, yellow intermediate cycles, and red represents later cycles.

Toward the end of the PFR investigation, during final life cycle testing of the hardware, audible sound was observed from the hardware. This sound triggered further investigation and resulted in the development of an assembly-level relubrication process for the mechanisms. This procedure eliminated the source of the concerning noise. The relubrication process seeks to augment lubrication in areas on the sleeve bearing where lubricant may have worn away during mechanical cycling.

3.4 Resolution for Traditional Mechanisms

Following resolution of the hardware failure, all flight spring assemblies have been updated, passed flight acceptance environmental testing, and have been integrated into both SWOT and NISAR flight masts. The mechanisms have successfully been tested at higher levels of

assembly and performance is consistent. Based on the process developed in the hardware failure investigation, the spring mechanisms require relubrication every 8 cycles of ground testing, which is achievable at the integrated level of assembly.

Key lessons learned from the development of these torsion springs:

- Avoid rectangular cross section springs unless volume limitations necessitate their use. Round wire springs have greater geometric and performance consistency and are simpler to analytically model.
- Beware of analytical model simplifications that may oversimplify and invalidate the results.
- Rectangular cross section springs will twist about the axis of the wire when wound. This twisting needs to be considered when designing any hardware coming in contact with the spring.
- Consider both the wound and unwound geometry of the spring during design of the mechanism. [12] [13]

CHAPTER 4

SPRING THEORY

In an attempt to alleviate the issues encountered with the traditionally fabricated spring mechanism, the application of additive manufacturing will be studied to improve torque performance, mass, and volume. Torsion springs are generally cold wound or machined. As such, spring design has generally been limited to round or rectangular cross sections. This is because most applications allow for an increase in stock wire size if performance is not adequate. As previously stated, for the SWOT and NISAR missions, the spring design was driven by volume limitations. Therefore, notably increasing the size of the spring to improve torque output was not possible.

4.1 Spring Design Methodology

A torsion spring can be modeled as a beam undergoing constant moment. Therefore, the max stress in the beam can be modeled using equation 1. Variable K represents the Wahl stress concentration factor defined in equation 2. This is an analytically derived factor that accounts for increased stress in equation 1 due the effect of direct shear and change in spring coil curvature. The stress concentration factor is based on the spring index, the ratio of spring coil diameter to wire diameter.

$$\sigma = K \frac{Mc}{I} \quad (1)$$

$$K = \frac{3C^2 - C - 0.8}{3C(C-1)} \quad (2)$$

Using beam theory, the deflection of the spring can be calculated using equation 3. Here, moment is replaced with the equivalent force multiplied by length of the spring wire.

$$\theta_e = \frac{y}{l} = \frac{Fl^2}{3EI} \quad (3)$$

However, the spring end conditions must also be accounted for. The deflection of the cantilevered beams (for straight torsion spring arms) can be accounted for using equation 4. Where l_1 and l_2 represent the length of the torsion spring ends.

$$\theta_1 = \frac{Ml_1^2}{3EI} \quad \theta_2 = \frac{Ml_2^2}{3EI} \quad (4)$$

Ultimately, the total deflection of the spring can be calculated by summing equation 3 and 4.

$$\theta_T = \theta_1 + \theta_2 + \theta_e \quad (5)$$

The spring rate can now be calculated using equation 6.

$$k = \frac{Fr}{\theta_T} = \frac{M}{\theta_T} \quad (6)$$

With this formulation, springs can be designed without being limited to round and rectangular cross sections. For our purposes, the assumption of round wire is not useful. Additive manufacturing enables any cross-section to be considered. [14] [15]

4.2 Spring Design Considerations

The SWOT and NISAR mechanisms must output greater than 28 in*lbs of torque over 180 degrees of displacement. Therefore, the mechanism is rotationally preloaded to operate within the range of this performance. General aerospace mechanism design practices, as well as JPL best practices, require redundant torsion springs unless the mechanism can be proved reliable otherwise. Therefore, a baseline design of two redundant torsion springs is assumed. Ultimately, this requires that each spring must output a minimum of 19.8 in*lbs over the full functional range of motion.

4.3 Spring Design Software

Understanding the basics of spring theory is fundamental to being able to creatively leverage new manufacturing methods. However, software, such as “Advanced Spring Design 7,” is the industry standard in spring design. This software was used to design the springs that will fly on the SWOT and NISAR missions. This software was also used to iterate on various designs for AM springs quickly. Fundamentally, the software carries out the calculations described in previous sections. Appendix B displays an example of the software as used to design and analyze AM springs.

CHAPTER 5

DESIGN FOR ADDITIVE MANUFACTURING

Design for AM requires the simultaneous consideration of mechanism design, process design, and material consideration. All three areas must be considered and iterated upon to successfully leverage the full potential of AM for any application.

5.1 Material and Process Selection

Because of the myriad of AM processes, the range of possible AM materials use for compliant mechanisms is vast. The scope shall be narrowed to Direct Energy Deposition (DED) and Laser Bed Powder Fusion (LBPF) processes and materials that can be printed with these methods. DED and LBPF are the most developed AM processes for aerospace applications as far as material development, processes maturity, quality control, and manufacturing availability. Other processes were not considered for various reasons related to strength and durability. For example, ultrasonic additive manufacturing does not print hard metals easily, and binder jetting is expected to result in a lower porosity than LBPF.

For this study, material properties will be assumed based on available literature. A list of materials considered compared to traditional spring materials is shown in Appendix C. Ultimately, EOS MS1 Maraging steel was selected because of its high performance and similar behavior to the flight material. Table 2 compares traditional spring material to EOS MS 1. Any AM hardware developed for space flight will need go through the process of validating material properties based on required standards.

Table 2. *Traditional flight hardware material compared to AM EOS MS1. [16]*

	17-7 CH900	EOS MS1
Elastic Modulus (Pa)	2.04E+11	1.80E+20
Yield (Pa)	1.93E+09	1.99E+09
Ultimate (Pa)	2.01E+09	2.04E+09

A specific consideration for material and process selection is fatigue life. The original spring had a much higher fatigue life ($>10,000$ cycles) than needed. In application, the mechanism is only deployed once in space. However, during the integration and testing of the mechanism, the spring may see roughly 20 cycles. AM generally is assumed to result in lower fatigue life compared to traditional materials because of the assumed higher surface roughness and the increased possibility of subsurface defect. [17] Therefore, for a torsion spring, the engineering trade to exchange fatigue life for design flexibility must be evaluated.

5.2 Spring Design


Leveraging AM, many types of cross-sections are now possible to fabricate for all types of springs. For mass sensitive applications, hollow springs may be used. In this application, torque performance and volume are the driving design factors. To maximize cross-sectional moment of inertia, an I-beam section may be leveraged. However, for small springs, this design becomes less attractive when considering complications due to friction between windings of a torsion spring. Remaining with a rectangular cross section, AM enables a higher cross-sectional aspect ratio than otherwise possible with the current state of the art of cold wound springs. By increasing the height of the rectangular section from 5.33 mm to 7mm while minimizing the section width from 1.4 to 1.2 mm, stress decreases notably if torque output is held constant. Further, the ability to round corners and surfaces of the cross-section alleviates the issues experienced with the traditional mechanism.

Using Advanced Spring Design 7 software, several springs were designed and analyzed in preparation for manufacturing. These springs are shown in Table 3 compared to the “baseline” spring that will fly on the SWOT and NISAR missions. The springs analyzed were incrementally changed with respect to each other. Because of budgetary constraints, not all springs were manufactured. This will be discussed in following sections. These spring designs are also outlined in detail in Appendix A. Changes in cross-section height do not result in prohibitive change in stress margin while maintaining required torque performance and safety factors. For all designs, 27.25 spring body windings were used.

For round wire torsion springs, “line” contact is formed between the windings. For rectangular contact springs, “surface” contact is formed between the windings, increasing friction. However, with AM, rectangular cross-sections can be modified to minimize contact between

windings. “Standoff” features can also be added to remove surface rubbing and form line contact between windings. This can be seen in the final design of Table 3.

Table 3. *Summary of design variables for springs tested.*

					
	5.33mm	5.33mm	7 mm	9 mm	7 mm
	1.4mm	1.4mm	1.4mm	1.4mm	1.2mm
	Baseline	1:1 Swap	Increase Radial Height Step 1	Increased Radial Height Step 2	Minimized Thickness, Increased Height
Material	17-7 PH CH900	EOS MS1	EOS MS1	EOS MS1	EOS MS1
Spring Constant (in*lb/deg)	0.16	0.14	0.31	0.63	0.27
Displacement at 20 in*lb/deg (degrees)	123	139	64	32	75
Max Torque Out (180 deg past minimum torque needed) (in*lb/deg)	49	46	76	133	68
Yield Stress Margin (% , 1.5 FOS)	53%	69%	76%	66%	69%
Ultimate Stress Margin (% , 1.65 FOS)	45%	58%	65%	56%	58%

CHAPTER 6

MANUFACTURING AND TESTING

6.1 Manufacturing Preparation

Once springs were designed, drawings for AM hardware needed to be generated. Standard drawing notes have been developed for traditional manufacturing methods, along with standard material allowables. However, process controls for additive manufacturing are largely left to the engineer until engineering organizations establish which of the burgeoning AM processes and standards they wish to use. Notably, the American Society of Mechanical Engineers (ASME) and the International Organization for Standardization (ISO) have both developed some standards for AM. [18] [19] [20] The America Makes Consortium has also aggregated AM standards and identified where design and process standards are lacking. [21] [22] Upcoming NASA standards will address the lack of design standards for mission critical aerospace hardware. [23] Appendix A contains the drawings created for this project. These drawings include structurally embedded torsion springs that will be discussed in later sections.

6.2 Manufacturing and Inspection

The springs were fabricated on EOS LBPf printers at two vendors. The vendors each applied proprietary printing parameters and heat treat to the EOS MS1 Material. Print quality varied greatly between vendors. Figure 12 shows the visual difference as a result of different heat treat methods. Vendor #1 had previous experience using maraging steel powder, and had developed custom parameters for their EOS M290 printers. The springs were fabricated using powder from Carpenter Additive with a particle size distribution (PSD) between 15-45 μm . Layer size was 40 μm . After printing, the springs were heat treated at 490°C for 6 hours in air. Specific print details from Vendor #2 were kept proprietary. However, it is expected that standard EOS parameters were used for EOS MS1 powder. These parameters can be found publicly.

Inspection of the as-printed hardware displays various print defects. Interestingly, print defect types differ between vendors. Vendor #1's springs primarily display defects generated by the printing process itself. Figure 14 displays these defects. Vendor #2's defects appear to have been generated by the post-processing of the hardware and are shown in Figure 15.

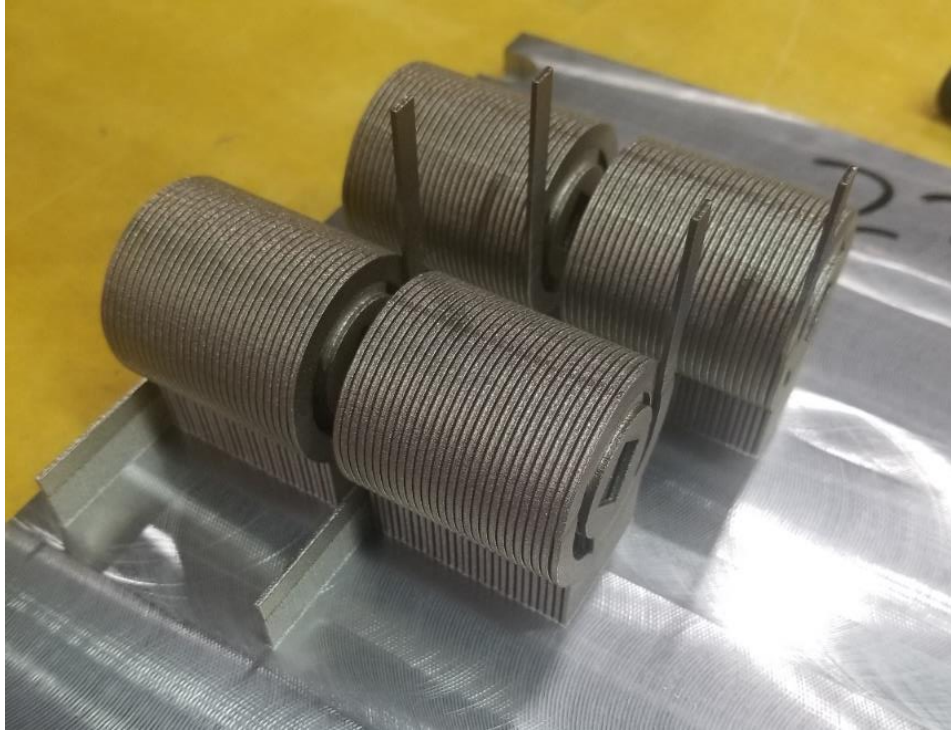


Figure 12. As printed springs from Vendor #1 shown before support material removal.

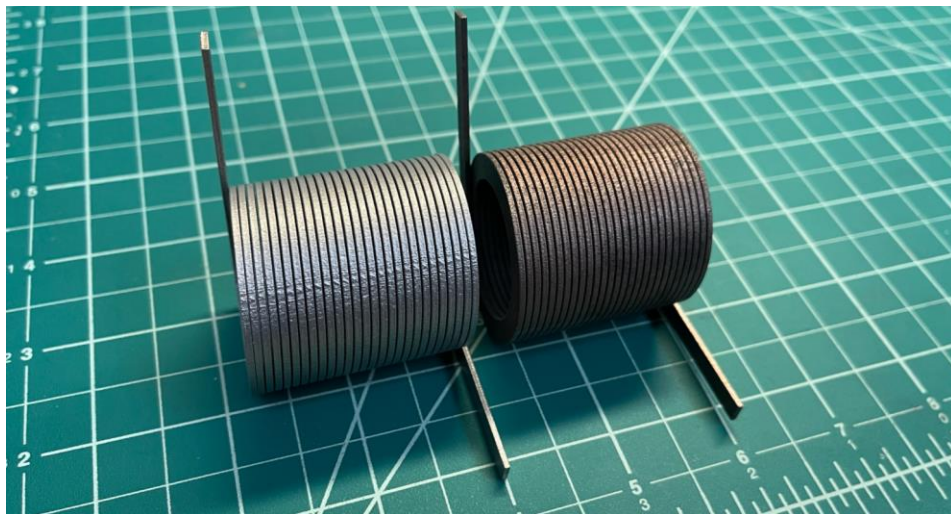


Figure 13. Vendor #1 spring (left) and Vendor #2 spring (right).

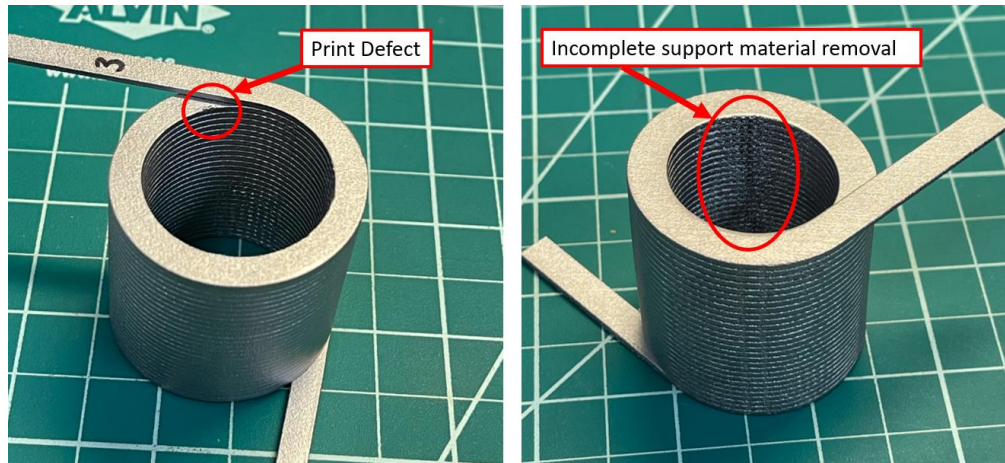


Figure 14. Defects upon inspection of a spring from AM Vendor 1.

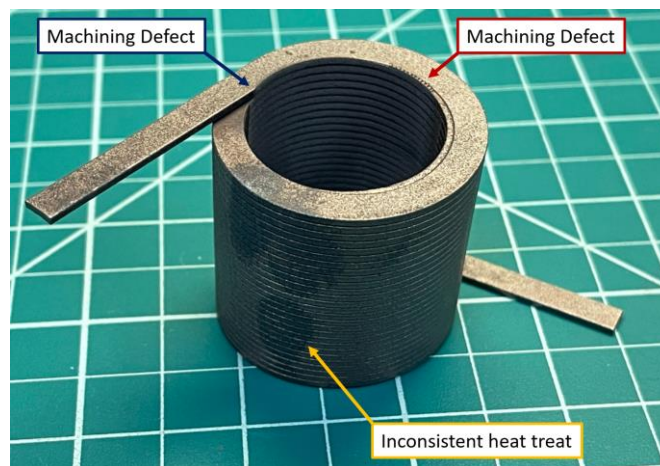


Figure 15. Defects upon inspection of a spring from AM Vendor 2.

Dimensional inspection allows for insights into the repeatability of printing this material as well as the geometric tolerances of the as-printed parts. Of all the dimensions printed, the vast majority of dimensions met tolerance requirements, matching those of the traditionally fabricated spring. Furthermore, when comparing the masses of the traditionally fabricated springs to that of the AM springs with similar geometries, the masses were proportional to differences in material density. The AM spring on average weighed 0.406 lb (EOS MS1 material density of .289 lb/in³) and the traditional spring weighed 0.399 lb (17-7 steel material density of 0.282 lb/in³).

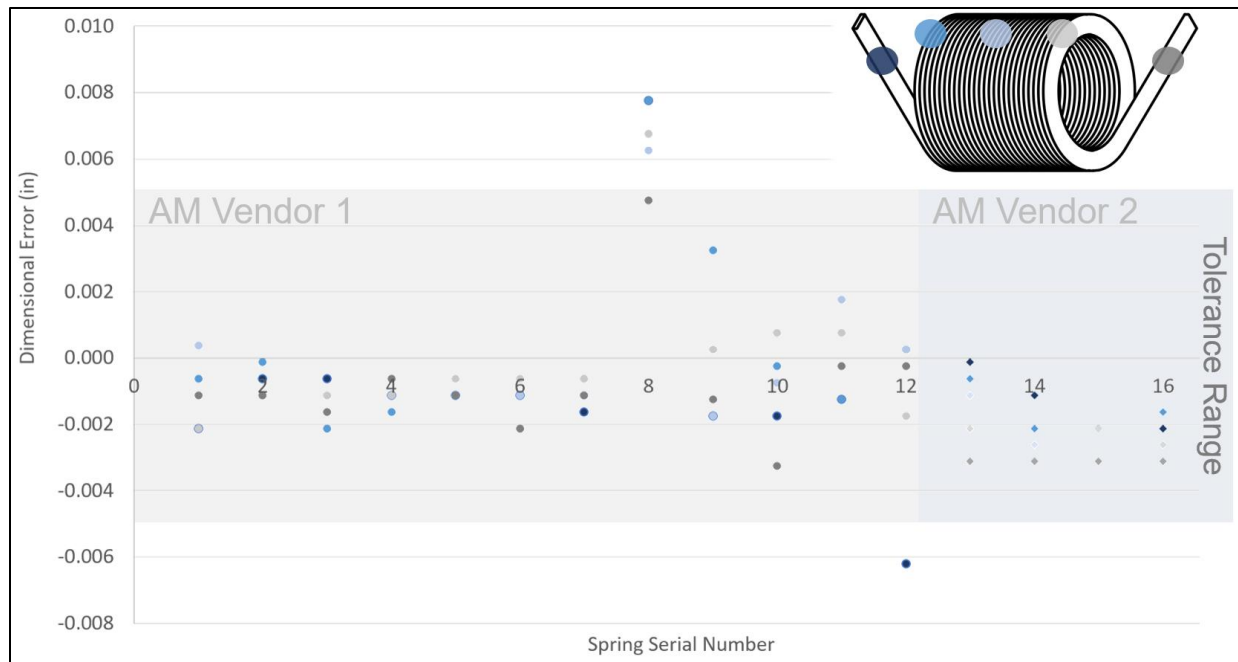


Figure 16. Dimensional inspection of cross section error for spring winding width. This inspection demonstrates that most as-fabricated springs achieve required geometric tolerances for winding width.

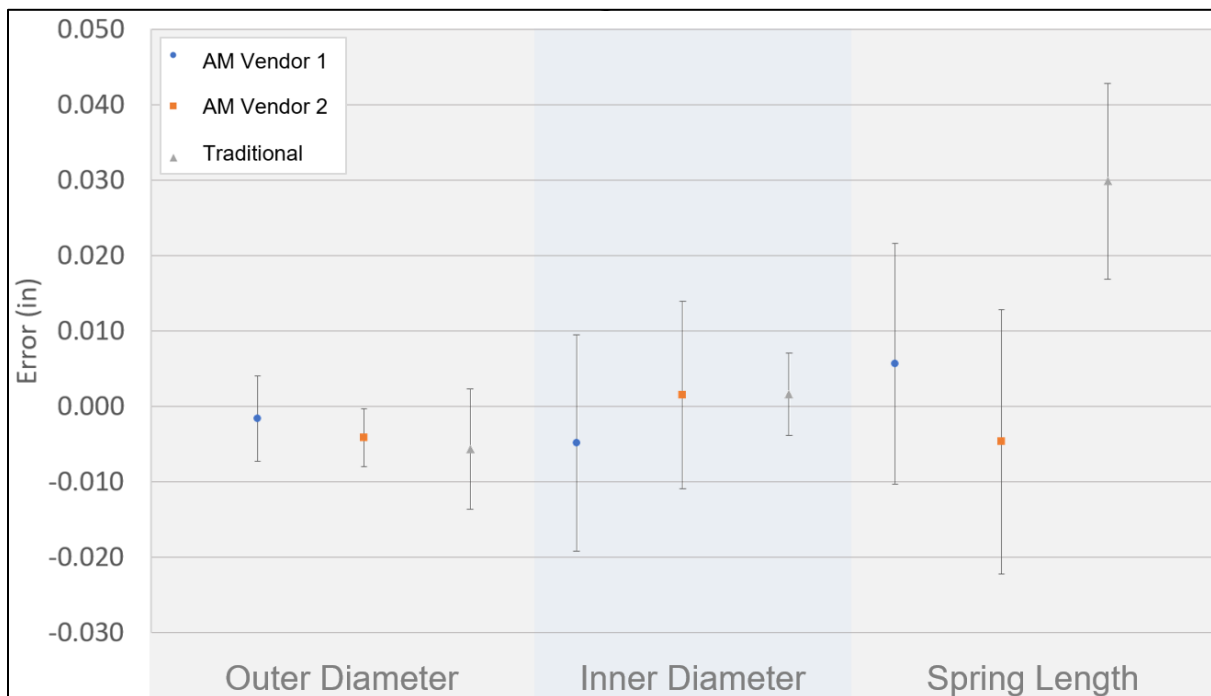


Figure 17. Inspection of spring major dimensions. This inspection demonstrated that all AM parts as fabricated achieve required geometric tolerances for major dimensions.

6.3 Experimental Test Setup

To test the spring torque performance, a bench top test setup was built utilizing a hand-held calibrated torque dial and custom tooling mounted to an optical bench. Figure 18 shows the test setup. This test setup allowed the axis of rotation to remain unconstrained, but allowed the upper spring arm to be driven with a measured torque value. The torque dial used had an uncertainty of 2.5 in*lbs.

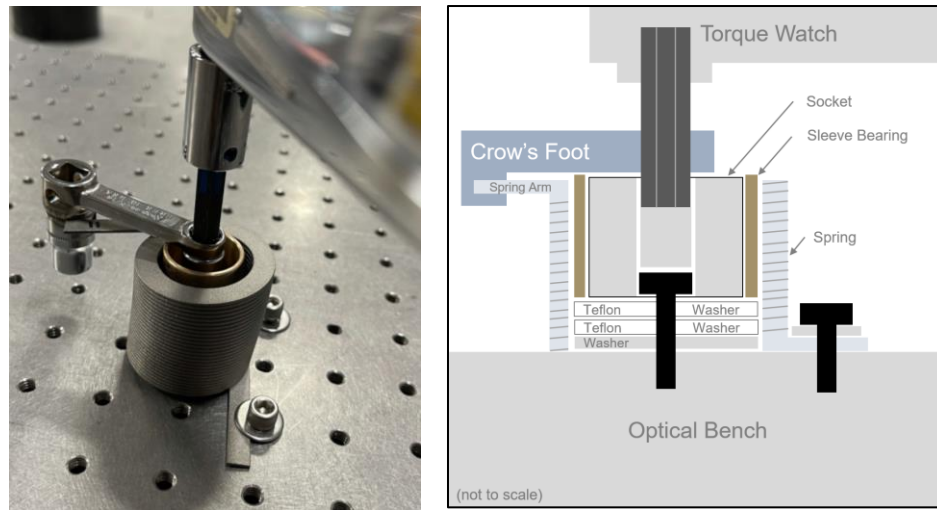


Figure 18. Experimental test setup for measuring spring torque performance.

6.4 Torque and Life-Cycle Testing Results

To test the performance of the AM springs, a series of springs were manufactured that incrementally differed from the traditionally fabricated spring. This will allow each design change to be studied incrementally. Sixteen additively manufactured springs were tested and compared to six traditionally manufactured springs in the same bench-top test setup. This allowed performance to be compared directly. Table 4 summarizes the test results. Figure 19 provides a visual representation of torque output with respect to displacement. For all springs, experimental performance slightly exceeded design performance. The spring with increased radial height showed a 148% increase in torque output at 270 degrees of displacement and a 117% increase spring constant compared to the flight spring. Four units of each spring design were tested and

with a standard deviation of 3.8 in*lbs or less for each design. Higher standard deviations were generally associated with higher displacement measurements.

Additionally, life-cycle testing was conducted on two of the springs. Life-cycle testing is defined as functional testing through at least three times the number of expected cycles needed in application. For the SWOT and NISAR missions, roughly 20 cycles of the spring mechanism are needed for ground testing and flight applications. Therefore, a lifecycle test must apply at least 60 cycles on the springs. Two springs were tested through 80 cycles of winding and unwinding, no degradation in torque was witnessed.

Table 4. Spring Torque Performance Test Results.

	Baseline	1:1 Swap (Vendor A)	1:1 Swap (Vendor A)	Increase Radial Height	Thickness change, Increased Height, Friction Feature
Manufacturer	Tradition al Vendor	AM Vendor 1	AM Vendor 2	AM Vendor 1	AM Vendor 1
Quantity tested	6	4	4	4	4
Material	17-7 PH CH900	EOS MS1	EOS MS1	EOS MS1	EOS MS1
Cross-Section Width, Axial (mm)	1.40	1.40	1.40	1.40	1.20
Cross-Section Height, Radial (mm)	5.33	5.33	5.33	7.00	7.00
Design Spring Constant (in*lbs/deg)	0.150	0.144	0.144	0.312	0.267
Experimental Spring Constant (in*lbs/deg)	0.177	0.173	0.176	0.383	0.330
% experimental spring constant compared from design	+18%	+20%	+22%	+22%	+24%
% spring constant experimental compared to baseline	0.00%	-2.2%	-0.56%	+76%	+50%

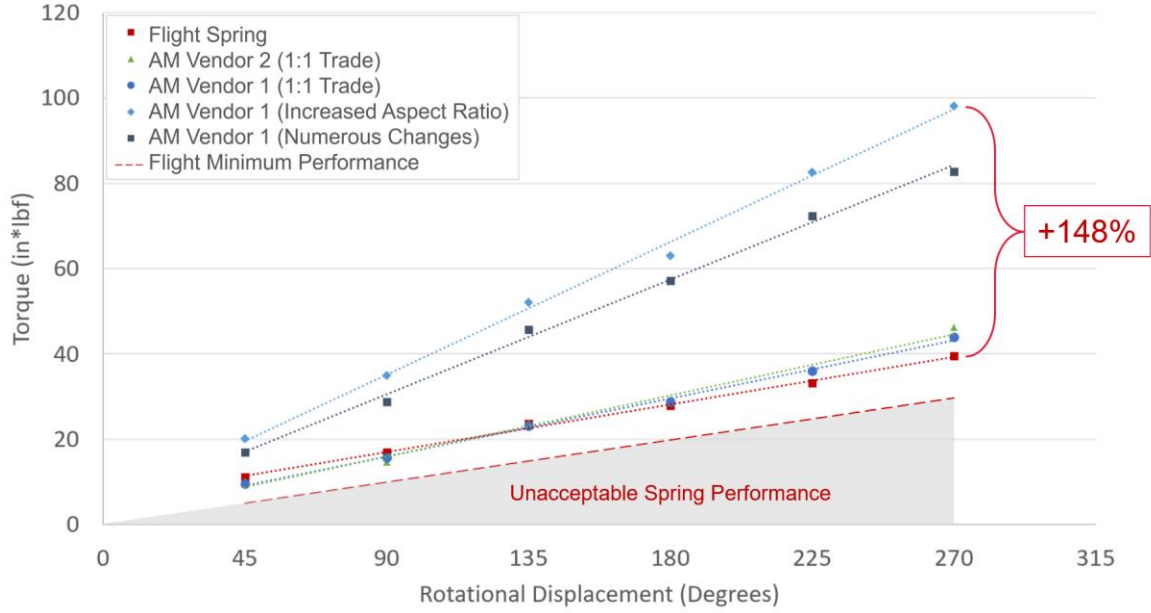


Figure 19. Average spring torque output with respect to displacement.

6.5 Material Testing

During printing at AM Vendor #1, twelve tensile coupons were printed from two lots of printed springs, six coupons from each lot. These tensile coupons were then machined down and tensile tested to failure per ASTM E8 “Standard Test Methods for Tension Testing of Metallic Materials.” Figure 20 shows the tensile coupons before and after machining. Testing results were slightly lower than expected material properties. Table 5 summarizes the testing results. These results would need to be studied further to determine the cause of the differences. A larger data set would be needed to create reliable material allowables. Heat treat, print parameters, and print orientation are a few of the possible variables that could affect the outcome.

Table 5. Tensile test result summary.

	Units	As-Printed AM Maraging Steel	Expected AM MS1
Elastic Modulus	10^3 ksi	25.6	26.1
Yield	ksi	290	288
Ultimate	ksi	293	297
Source		As-tested	Matweb [16]



Figure 20. Tensile coupons shown as printed and after machining.

CHAPTER 7

FUTURE IMPLICATIONS

Now that performance of AM torsion springs has been demonstrated, it is possible to extend the research in numerous significant ways. First, it is possible to minimize mass and volume by redesigning the springs. Second, it is possible to minimize part count drastically. Finally, further work is needed to increase the Technology Readiness Level (TRL).

Testing has demonstrated that for the SWOT and NISAR deployment springs a 1.2mm x 7mm cross-section allows for increased torque performance while maintaining necessary stress margins. With this information, it is possible to hold the spring cross-section constant, and modify the number of coils to minimize mass and volume while maintaining acceptable stress margins. As such, it is possible to manufacture a spring that has 17.25 body coils (seen in Figure 21), and maintains positive stress margin with the following performance:

- Decrease mass by 23% compared to flight hardware
- Decrease spring axial length by 52% compared to flight hardware
- Increase spring rate by 167% compared to flight hardware.

It should be noted that further testing will need to be carried out to ensure that frictional losses when fully integrated are not prohibitive.

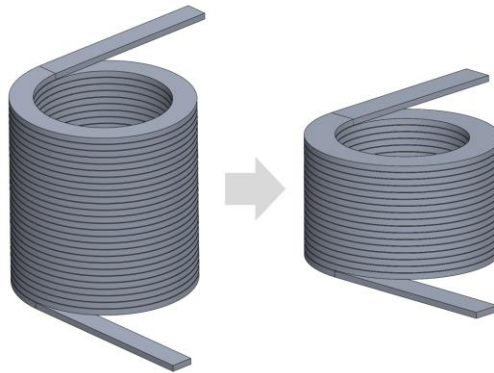


Figure 21. Flight spring design compared to zero stress margin AM spring design.

Part count can also be drastically minimized by embedding the spring in the surrounding structure. Using standard AM manufacturing, it is possible to minimize the part count from 24 parts to 9 parts in the spring mechanism. This is partially achieved by printing both springs in the same piece part. Thus, a single part remains redundant with two individual complaint elements. Figure 22 demonstrates this part reduction when compared to Figure 8. Technical drawings of this mechanism with minimized part count can be found in Appendix A. Part count reduction is also associated with decreased manufacturing, inspection, and testing costs. Further work will be needed to fully quantify possible cost savings. Using more advanced manufacturing techniques, it may be possible to monolithically print this hardware. This would require further study.

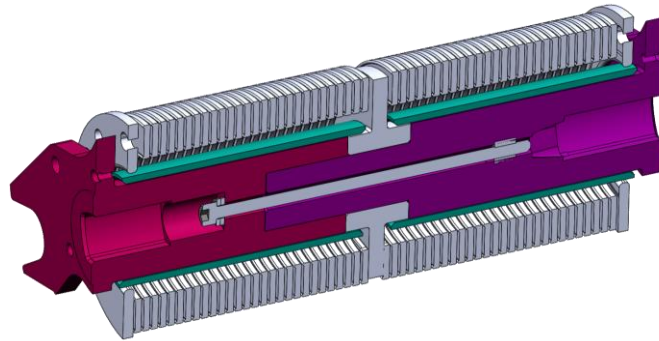


Figure 22. *Structurally embedded spring with nine total parts demonstrates reduction in part count when compared to traditional manufacturing methods.*

This report has demonstrated the use of AM springs at the component level in a laboratory environment. Thus, achieving a TRL level of 4. [24] However, further work is needed to mature the technology to be adopted onto a flight mission without increased risk to the mission. Specifically, the following areas should be studied to achieve TRL 6 or higher:

- A full environmental and life-cycle test campaign of the mechanism is needed to confirm findings in this report and achieve TRL 6.
- A standard process for NDI of AM compliant elements needs to be developed. This will allow confidence that printed parts do not have any unseen defects that could cause pre-mature failure. This is expected to be part of upcoming NASA AM design standards. [23]

- Post-processing manufacturing methods for AM compliant hardware (e.g., surface finishes, coatings, etc.) will need to be studied further for potential performance improvements. Specifically, decreasing as-printed surface roughness with chemical etching will likely increase hardware cycle life if high cycle life is needed. Further, corrosion resistant coatings will protect maraging steel hardware from stress fracture when exposed to corrosive environments.

Figure 23. AM Spring Drawing.

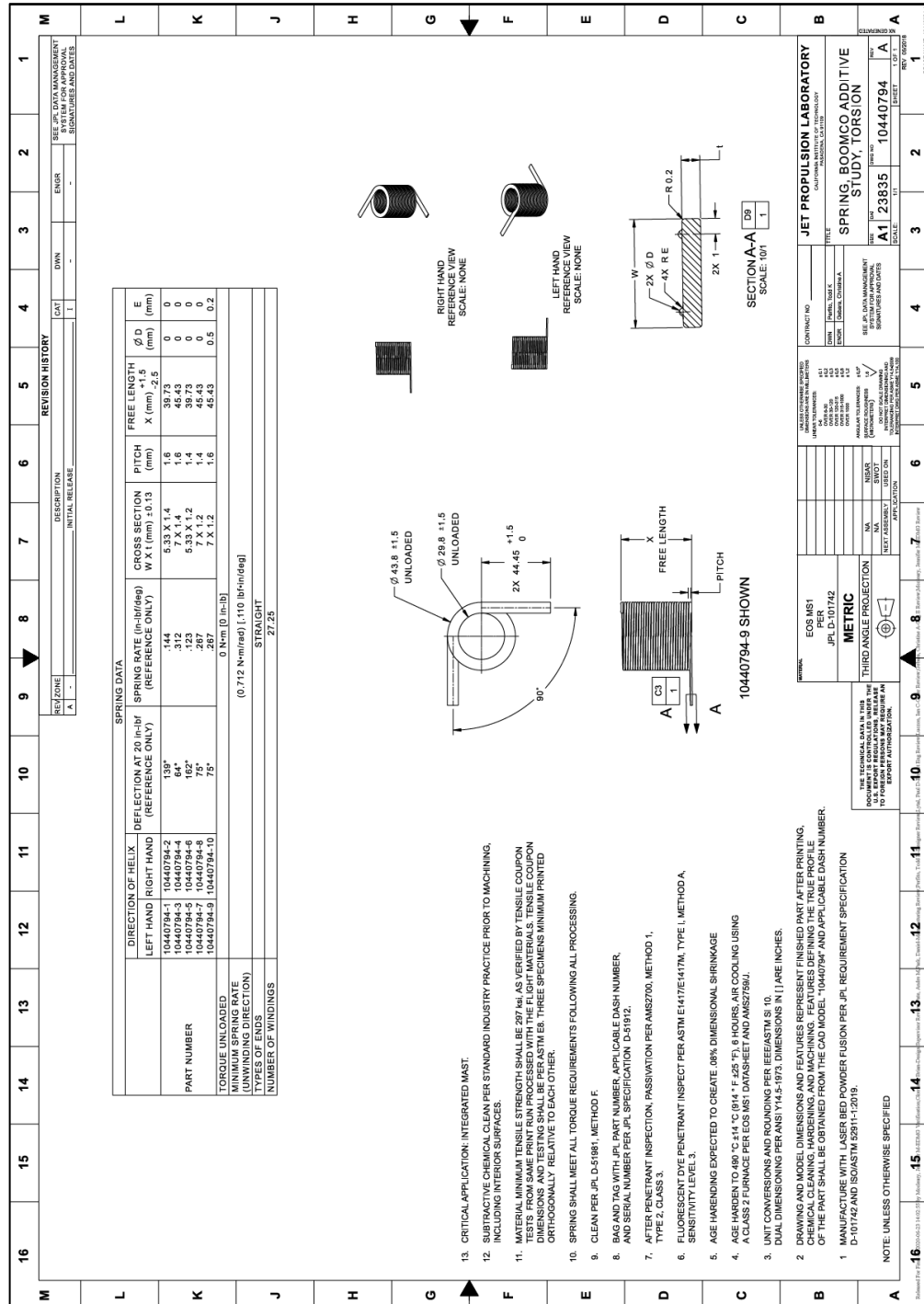


Figure 24. AM Structurally Embedded Spring Drawing.

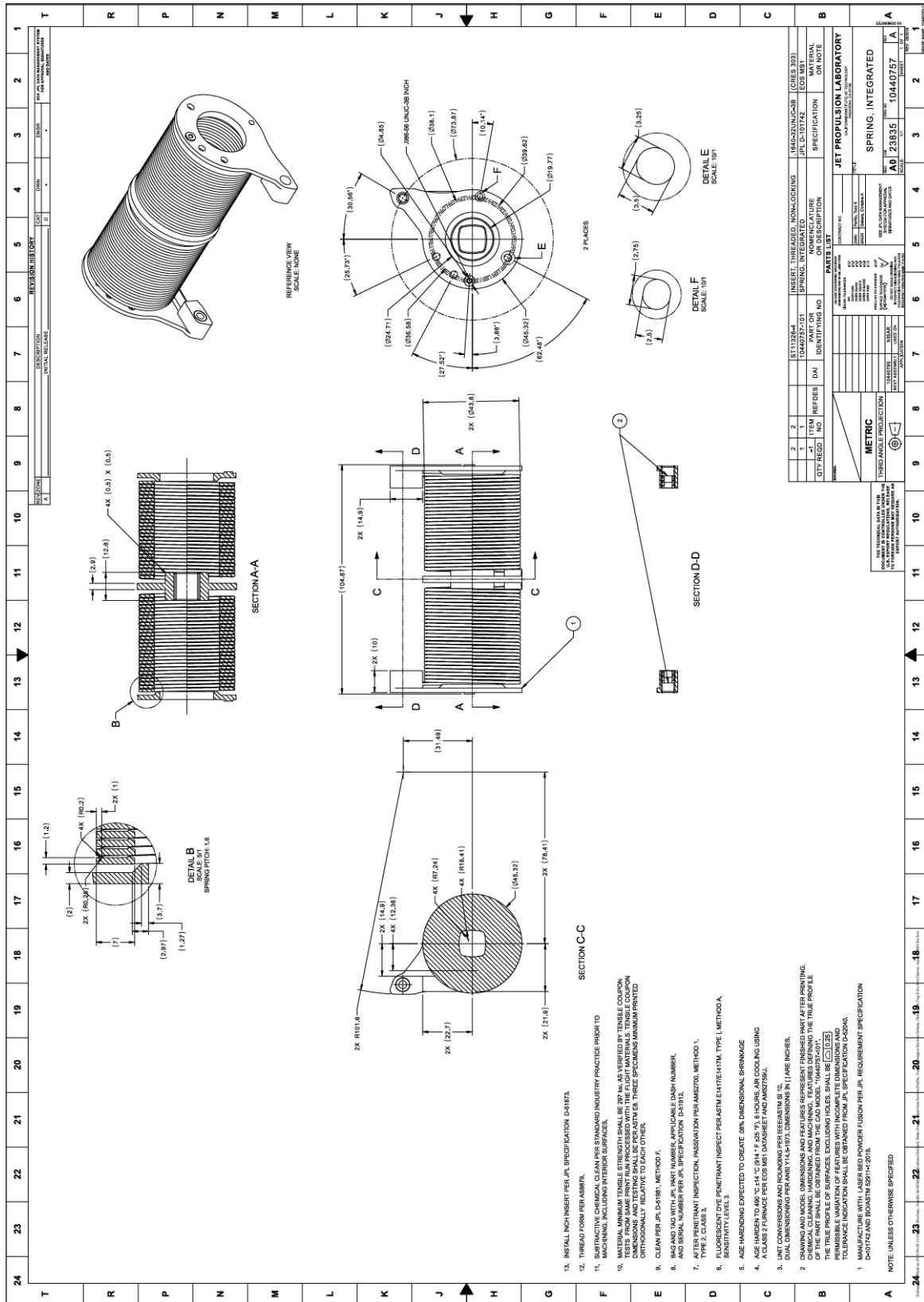
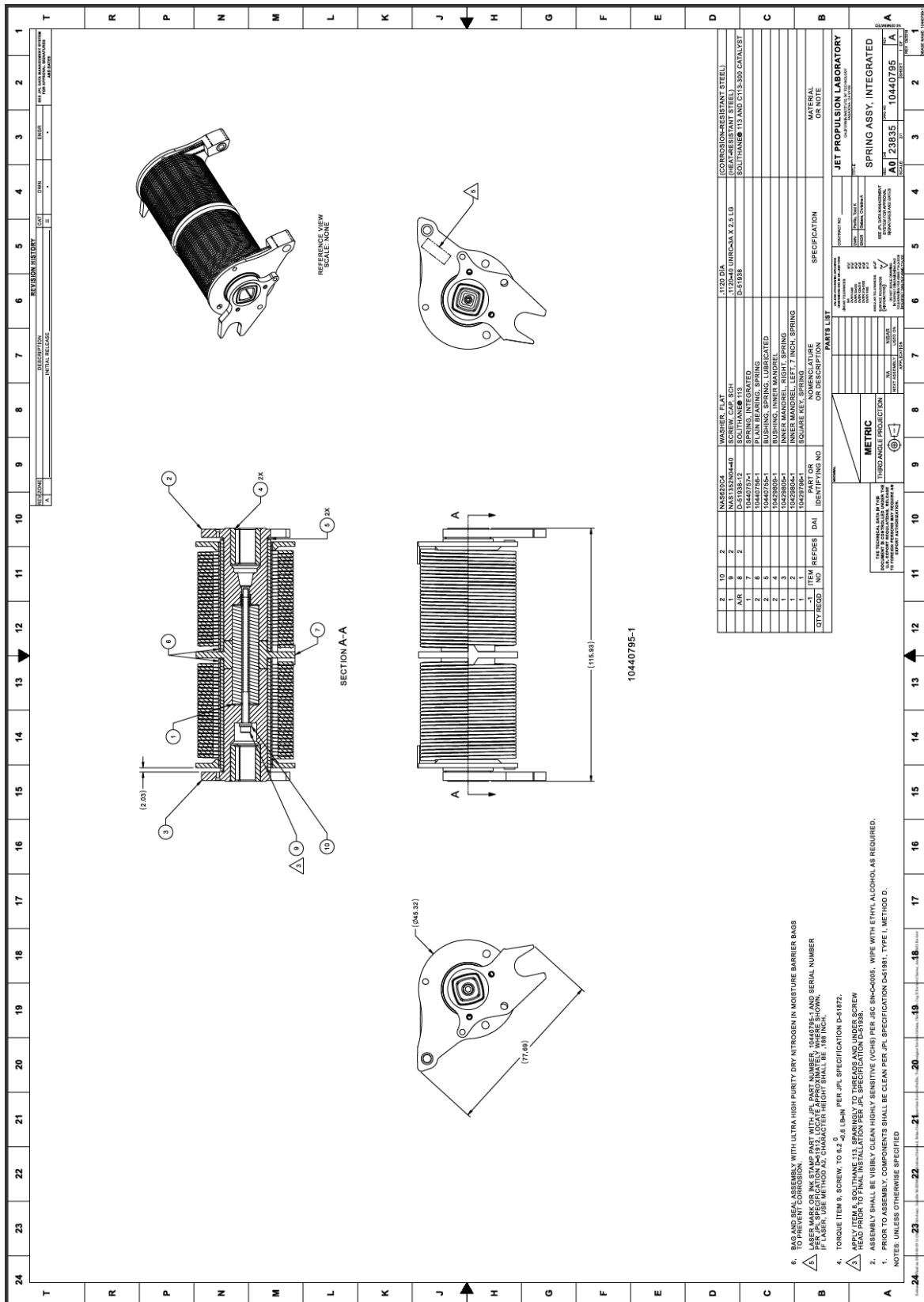


Figure 25. AM enabled spring mechanism drawing.



APPENDIX B: ADVANCED SPRING DESIGN SOFTWARE

Figure 26. Advanced Spring Design Software.

Torsion Spring - Standard - Rectangular Wire - NA

Material: EOS MS1 Round Grade: ☐ Commercial ☒ Precision

Configuration: ☒ Close Wound ☐ Pitched Coiling Direction: ☒ Optional ☐ Left ☐ Right

Input / Output Scenarios: ☒ Power User ☐ Standard ☐ Dimensional (Inputs for these two cases are indicated by green backgrounds)

☐ Shot Peened
☒ Equal Arm Lengths
☐ Use Wahl Factor
☒ Use Keystone Factor
☐ User-defined SN data

Note: *Italicized labels indicate optional inputs.*

Radial Wire Thickness	0.3543 in	Coil ID	1.2059 in	Pitch	0.0589 in
Axial Wire Thickness	0.0551 in	Coil Mean Diameter	1.5602 in	Additional Feed	0.0000 in
Wire Length	136.5872 in	Coil OD	1.9145 in	Allowable Body Length	in
Wire Weight	0.781269 lb	Coil Dia. Tol. (+/-)	0.0200 in	Support Shaft Diameter	1.0700 in
Minimum Tensile Strength (MTS)	1000 psi	Minimum Coil ID	1.1859 in	Load Tol. (+/-)	5.7429 lbf-in
Spring Rate	0.6302 lbf-in/deg	Maximum Coil OD	1.9345 in	Free Angle Tol. (+/-)	9.1127 deg
Spring Index	4.4036	Moment Arm 1 Length	1.7504 in	Estimated Life Cycles	< 100000
		Moment Arm 2 Length	1.7504 in		

	Free	Cycle Torque 1	Cycle Torque 2	Other Torque	Set	
Torsional Moment	0	113.4374	272.2497	408.3746	1.1528	lbf-in
Contact Force, Arm 1	0	64.8065	155.5357	233.3036	0.6586	lbf
Contact Force, Arm 2	0	64.8065	155.5357	233.3036	0.6586	lbf
Moving Arm's Angle	54.0000	234.0000	126.0000	342.0000	55.8292	deg
Angle Between Arms	126.0000	306.0000	54.0000	198.0000	124.1708	deg
Deflection	0	180.0000	432.0000	648.0000	1.8292	deg
ID Stress	0	98404	236170	354255		psi
OD Stress	0	98404	236170	354255		psi
% of Min. Tensile Strength	0	9840.4	23617.0	35425.5	100.0	
Body Coils	27.1500	27.6500	28.3500	28.9500	27.1551	
Active Coils	27.3881					
Body Length	1.6581	1.6875	1.7288	1.7641		in
Min. Coil ID		1.1577	1.1199	1.0889	1.1856	in

Wire Available:
 Next Smaller Wire Size:
 Next Larger Wire Size:

APPENDIX C: AM MATERIAL COMPARISON

Table 6. Material comparison.

Process	Mat'l	Post Processing	Elastic Modulus		Yield		Ultimate		Material chosen for flight
			KSI	GPa	KSI	MPa	KSI	MPa	
Traditional	17-7PH CH900 (tested allowables)	Precipitation-hardened CH900	29600	240	279.6	1927.8	291.8	2011.9	AM Materials
LPBF	EOS MS1	Age Hardening	26000	180 ± 20	289 ± 15	1990 ± 100	297.2	2049	
LPBF	Oerlikon C300 – Maraging Steel	Heat Treatment	Unknown	Unknown	287.2	1980 ± 7	294	2027 ± 9	Traditional Materials
DED	Ti-6Al-4V	As-built	Unkwn	Unkwn	168.49	1162	182.7	1260	
LPBF	AlSi10Mg, 6h 200 C	6h/200 °C	Unkwn	Unkwn	37.7	260	49.3	340	
LPBF	17-4PH	PH	Unkwn	Unkwn	88.45	610	131.95	910	
LPBF	17-4 PH CA+H900	Precipitation-hardened CH900	Unkwn	Unkwn	196.04	1352	209.38	1444	
LPBF	17-4 PH	PH 788C for 2 h + H900	Unkwn	Unkwn	163.27	1126	211.265	1457	
LPBF	Ti-6Al-4V	650°C, 4 hrs. in Ar; furnace cool to room temperature	Unkwn	Unkwn	165.735	1143	176.755	1219	
LPBF	AlSi10Mg	As-built	Unkwn	Unkwn	37.7	260	54.375	375	
LPBF	Ti-6Al-4V	As-built	Unkwn	Unkwn	174	1200	188.5	1300	Traditional Materials
Traditional	17-7PH CH900 (published allowables)	Precipitation-hardened CH900	29600	240	230	1586	240	1655	
Traditional	Ti-6Al-4V	None	Unkwn	Unkwn	129.92	896	145	1000	
Traditional	AlSi10Mg	High Pressure Die Casting Heat Treatment	Unkwn	Unkwn	41.325	285	47.85	330	
Traditional	CRES 302	Annealed	28300	195	39.875	275	89.9	620	
Traditional	Ti 3Al-8V-6Cr-4Mo-4Zr (Ti Beta C)		15100	104	162	1120	177000	1220	
Traditional	13V-11Cr-3Al	Solution Treated	14359 (tensile)	99 (tensile)	162	830	143.55	990	

REFERENCES

- [1] Wholers, T., and Gormet, T., “History of Additive Manufacturing,” *Wholers Report*, 2015, <http://www.wohlersassociates.com/history2014.pdf> [cited 8 December 2019].
- [2] “Aerojet Rocketdyne’s Family of 3d-Printed Rocket Engines,” Aerojet Rocketdyne, 2019, <https://www.rocket.com/innovation/bantam> [cited 8 December 2019].
- [3] “SpaceX Launches 3d-Printed Part To Space, Creates Printed Engine Chamber,” SpaceX, 2014, <https://www.spacex.com/news/2014/07/31/spacex-launches-3d-printed-part-space-creates-printed-engine-chamber-crewed> [cited 8 December 2019].
- [4] Palmer, Annie, “NASA uses AI software to create radical interplanetary lander that could one day touch down on the moons of Saturn or Jupiter,” *The Daily Mail UK*, 2018, <https://www.dailymail.co.uk/sciencetech/article-6391139/NASA-uses-AI-software-create-lander-touch-Saturn-Jupiters-moons.html> [cited 8 December 2019].
- [5] “Case Study PIXL Mars Rover,” Carpenter Additive, 2020, https://f.hubspotusercontent10.net/hubfs/6205315/Resources/Case%20Study/20210122-CT-Mars-Rover-Case-Study_F.pdf?hsCtaTracking=aa07829b-5b60-474e-92de-36d99da655f7%7C41643ab9-681e-4065-9066-4362fc3a85dd [cited 12 April 2021].
- [6] “Mars 2020 Mission Perseverance Rover Raw Images,” National Aeronautics and Space Administration, 2020, <https://mars.nasa.gov/mars2020/multimedia/raw-images/> [cited 12 April 2021].
- [7] “Radar in a CubeSat (RainCube),” *NASA JPL*, 2018, <https://www.jpl.nasa.gov/cubesat/missions/raincube.php> [cited 8 December 2019].
- [8] “LightSail,” *The Planetary Society*, 2019, <https://www.planetary.org/explore/projects/lightsail-solar-sailing/> [cited 8 December 2019].
- [9] Jeon, S., and Murphey, T., “Design And Analysis of A Meter-Class Cubesat Boom with A Motor-Less Deployment by Bi-Stable Tape Springs,” *AIAA Structures, Structural Dynamics, and Materials Conference*, 2011, <https://arc.aiaa.org/doi/pdf/10.2514/6.2011-1731>.
- [10] “Overview,” National Aeronautics and Space Administration, 2020, <https://swot.jpl.nasa.gov/mission/overview/> [cited 12 April 2021].
- [11] “Mission Concept,” National Aeronautics and Space Administration, 2020, <https://nisar.jpl.nasa.gov/mission/mission-concept/> [cited 12 April 2021].

- [12] Lytal, P., and Renson, M., “Spacecraft Common Deployable Boom Hinge Deploy and Latching Mechanisms,” Proceedings of the 44th Aerospace Mechanism Symposium, 2017, 403-416.
- [13] Gebara, C., and Lytal, P., “Multi-Mission Deployable Boom: Spring Mechanism Failure Investigation and Solution,” Proceedings of the 45th Aerospace Mechanism Symposium, 2020.
- [14] Budynas, R.G., and Nisbett, J.K., “Shigley’s Mechanical Engineering Design,” Ninth edition, 2008, McGraw-Hill, New York, New York.
- [15] Wahl, A. M., “Mechanical Springs,” First Edition, 1944, Penton Publication Company, Cleveland, Ohio, USA.
- [16] “EOS MS1 Maraging Steel Sintered on EOSINT M 270.” MatWeb Material Property Data. Matweb LLC.
<http://www.matweb.com/search/DataSheet.aspx?MatGUID=e9f7cb19eb81450d8f67966151bd1802&ckck=1#:~:text=EOS%20Maraging%20Steel%20MS1%20is,obtain%20excellent%20hardness%20and%20strength.>
- [17] Debroy, T. et al., “Additive manufacturing of metallic components – Process, structure and properties,” Progress in Materials Science, Vol 92, March 2018,
<https://www.sciencedirect.com/science/article/pii/S0079642517301172#!> [cited 12 April 2021].
- [18] “ISO-ASTM52911-1-19 - Additive Manufacturing - Design - Part 1 - Laser-based powder bed fusion of metals,” ASTM International, 2019,
<https://www.astm.org/Standards/ISOASTM52911-1.htm> [cited 12 April 2021].
- [19] “ISO-ASTM52911-2-19 - Additive Manufacturing - Design - Part 2 - Laser-based powder bed fusion of metals,” ASTM International, 2019, <https://www.iso.org/standard/72951.html> [cited 12 April 2021].
- [20] “ISO-ASTM52910-18 Additive manufacturing – Design - Requirements, guidelines and recommendations,” ASTM International, 2018,
<https://www.astm.org/Standards/ISOASTM52910.htm> [cited 12 April 2021].
- [21] “ANSI & America Makes - Standardization Roadmap for Additive Manufacturing 2018 Version 2.0,” America Makes, 2018,
https://share.ansi.org/Shared%20Documents/Standards%20Activities/AMSC/AMSC_Roadmap_June_2018.pdf [cited 12 April 2021].
- [22] “America Makes & ANSI Additive Manufacturing Standardization Collaborative (AMSC) Standards Landscape (version 2.0, June 2018),” America Makes, 2018,
https://share.ansi.org/Shared%20Documents/Standards%20Activities/AMSC/AMSC_Standards_Landscape_June_2018.pdf [cited 12 April 2021].

- [23] Lanigan, E., “A NASA Perspective on the Growing Role of In-Situ Process Monitoring in Managing Risk of AM Hardware,” NASA Marshall Space Flight Center, 2019, <https://ntrs.nasa.gov/api/citations/20200000032/downloads/20200000032.pdf> [cited 12 April 2021].
- [24] “Technology Readiness Level,” National Aeronautics and Space Administration, 2020, https://www.nasa.gov/directorates/heo/scan/engineering/technology/technology_readiness_level [cited 12 April 2021].